EXPERIMENTAL ANALYSIS OF THE FLOW FIELD IN A ROTATING "U" CHANNEL

Gallo M., Astarita T., Carlomagno G.M.
University of Naples "Federico II" – DIAS, P.le Tecchio 80, 80125 Naples, Italy

Keywords: *Gas turbine, rotating channel, U turn, Coriolis' force, Vortical field*

Abstract

Particle Image Velocimetry (PIV) experiments have been carried out to obtain visualizations and measurements of flow field in a square channel with a 180° sharp turn. This paper is focused on the study of the flow and vortical field in the turn region and, in order to study the influence of the rotation on the flow field inside the channel, tests both in stationary (absence of rotation) and rotating conditions have been performed. The results show that the rotation determines strong modifications of the flow and vortical field present in the turn region.

1 Introduction

It is well known that, to improve the thermodynamic efficiency of gas turbine engines, it is necessary to increase the gas entry temperature. Present advanced gas turbines operate at gas entry temperatures much higher than metal creeping temperatures and therefore require intensive cooling of their blades, especially in the early turbine stages. Generally, in order to obtain an efficient cooling of blades, film cooling is imposed on their external surface while forced convection is performed inside the blade. In the second case, cooling air from the compressor is supplied through the hub section into the blade interior and, after flowing through a serpentine passage, is discharged from the dust holes arranged in the tip zone and in the blade leading and/or trailing edge. The serpentine passage is made of several adjacent straight ducts, spanwise aligned and connected by 180° turns. The presence of these turns and the rotation of the blades cause strong modifications of the flow pattern due to the formation of secondary flows; therefore the knowledge and the analysis both of the main and secondary flow fields are of fundamental importance for the qualitative and quantitative understanding of the spatial distributions of the convective heat transfer coefficient present in the literature.

In stationary conditions (absence of rotation), many studies have been carried out, with various techniques, visualizations and measurements of the flow fields present in smooth channels with 180° sharp turn. Kiml et al. [1], by using the paraffin mist as a tracer, visualized, in the turn and in the outlet duct, the three-dimensional flow structures generated by the turn. Liou et al. [2] conducted Laser-Doppler Velocimetry (LDV) measurements in order to analyze the effect of divider thickness on fluid flows. Particle Image Velocimetry experiments have been performed by Son et al. [3] with the aim to study the high-Reynolds number turbulent flow and wall heat transfer characteristics. Schabacker et al. [4], by means of a stereoscopic digital PIV system, have measured all three velocity components simultaneously.

It is well known from the literature that, in absence of rotation, the turbulent flow in a straight square duct channel is characterized by the presence of small corner vortices which are due to the Reynolds stress anisotropy. These secondary flows tend to disappear just before the turn; indeed, the presence of the turn produces a low pressure zone near to the tip of the partition wall, then, at the inlet of the turn, the pressure gradient directed from the inner to the outer wall induces a secondary flow that moves from the outer wall to the inner one. In the bend, the centrifugal forces due to the curvature and the associated pressure gradient between the outer and inner surfaces promote the formation of two symmetric counter-rotating vortices that, to a certain extent, persist also in the straight duct downstream of the turn. Since these counter-rotating vortices convey cold fluid from the core towards the surfaces, an increase of the heat transfer, both in the turn and in the downstream duct, is obtained.

Others researchers analyzed the flow field in channels with a 180° sharp turn in presence of rotation in order to simulate the motion of coolant in internal passages of the rotating blades of modern gas turbine. Cheah et al. [5] performed velocity field measurements in a rotating U-ducts of strong curvature with the axis of rotation parallel to that of curvature, by using the laser-Doppler anemometry. With the same technique Iacovides et al. [6] and Liou et al. [7] measured the turbulent flow field in a square ended U-bend with the axis of rotation orthogonal to that of the curve and performed measurements of the local heat transfer coefficient with the aim to identify possible correlations. Brossard et al. [8] conducted PIV experiments in a channel with a geometry similar to the ones of the two last works cited, and analyzed the flow field in planes parallel to the divider wall and orthogonal to the axis of rotation.

Numerical analyses of the flow field evolution and of the heat transfer distribution for rotating channels with 180° sharp turn have been also performed. Al-Qahtani et al. [9] investigated the effects of rotation, turn and channel orientation with respect to the axis of rotation, on the flow field and heat transfer distributions. Su et al. [10] analysed the effects of channel aspect ratio, Reynolds number and buoyancy, on the flow behaviour and heat transfer. Murata et al. [11] studied how the interaction of secondary flows, induced by the sharp turn and Coriolis' force, affects the heat transfer. Iacovides et al. [12, 13] studied the mean and turbulent flow in rotating U-ducts of strong curvature, with the axis of rotation parallel to that of curvature.

The channel rotation gives rise to the Coriolis' force that completely changes the flow field and, hence, the distribution of the local heat transfer coefficient. In the case of a radially outward flow, the Coriolis force produces a secondary flow (in the form of a symmetric pair of secondary vortices) in the plane perpendicular to the main moving direction of the fluid. In this case, the Coriolis force pushes the particles in the centre of the channel towards the trailing wall; then the flow continues along the trailing wall in the direction of the side walls and finally gets back to the leading wall. When the flow is reversed, i.e. for a radially inward flow, it is only needed to change the role played by the leading surface with that of the trailing one and vice versa.

Another effect of the Coriolis' force is the asymmetry of the axial velocity profile that determines unstable flow condition at the trailing wall and stable flow condition at the leading wall [14, 15]. A recent numerical study [16] points out the presence of other secondary flows which are constituted by two symmetrical pairs of counter-rotating cells. Every pair is formed by a large cell close to the stable wall and an additional small cell near the unstable wall. By increasing the rotation number, the first cell tends to move towards the corner while the second one increases its strength and size. These secondary flows are generated by a balance between the axial pressure gradient and the Coriolis force.

In the turn region, according to the studies of Su et al. [10] and Iacovides et al. [6], the secondary flows formed in the first passage are overpowered by bend induced vortices. Indeed, due to the rotation in the turn, these authors have observed an increase of the size and the strength of the vortex near the leading wall at the expense of the one close the trailing wall.

The present work has a twofold objective: to perform accurate measurements of the mean flow fields in the turn region by means of the PIV technique and to realize, in the same region, a 3D reconstruction of the vortical field. This study is not only important to characterize and justify the spatial distributions of the convective heat transfer coefficient present in literature but is also relevant to validate computer programs used to study these complex flows.

2 Experimental set-up and technique

In the present section only the measurement technique of the flow fields is accurately described because the used experimental apparatus is practically the same described by the same authors in a previous work [17].

2.1 PIV measurements and technique

The relevant dimensionless numbers are the *Reynolds number Re* and the *Rotation number Ro* (which is the inverse of the *Rossby number*):

$$Re = \frac{\rho V D}{\mu} \tag{1}$$

$$Ro = \frac{\omega D}{V} \tag{2}$$

where: D is the channel hydraulic diameter, V is the fluid mean velocity, ω is the channel rotational speed, ρ and μ are the mass density and the dynamic viscosity coefficient of the fluid, respectively. The Reynolds number governs the static behaviour of the flow field in the channel, while *Ro* is a dimensionless measure of the Coriolis effects. The maximum error on Reynolds number and Rotation number evaluation is lower than ± 3% [18]. The experimental tests have been performed, for the static case at *Re*=20000, while for the rotating case at *Re*=20000 and *Ro*=0.3.

In Fig. 1 is shown a sketch of the test region of the channel with the adopted coordinate system while Tab. 1 resumes the nomenclature of the channel's walls used to describe, in the next section, the flow fields.

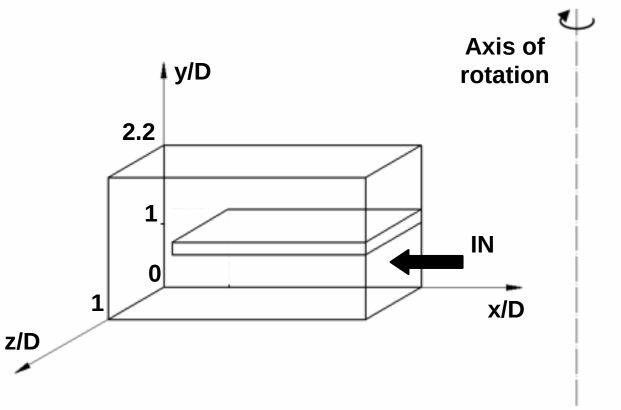

Fig. 1 Sketch of the test region.

Static Case		Rotating case	
Plane	**Name**	**Plane**	**Name**
z/D=0	Side wall	*z/D*=0	Leading wall
z/D=1	Side wall	*z/D*=1	Trailing wall
x/D=0	Frontal wall	*x/D*=0	Frontal wall
y/D=0	External wall	*y/D*=0	External wall
y/D=2.2	External wall	*y/D*=2.2	External wall

Tab. 1 Nomenclature of the channel's walls.

To reconstruct and analyze the tridimensional flow field in the turn region, PIV measurements have been performed in planes parallel to the three coordinate plane (*xy*, *yz*, *zx*). Tab. 2 reports all the investigated planes in the turn region both for the static and rotating case.

Static case				
Turn region	**Plane**	**From**	**To**	**Pitch**
Second half	*xy*	*z/D*=0.03	*z/D*=0.97	0.03*D*
	yz	*x/D*=0.08	*x/D*=1	0.17*D*
	zx	*y/D*=1.2	*y/D*=2.03	0.17*D*
Rotating case				
Turn region	**Plane**	**From**	**To**	**Pitch**
First half	*xy*	*z/D*=0.08	*z/D*=0.92	0.08*D*
	yz	*x/D*=0.17	*x/D*=1	0.17*D*
	zx	*y/D*=0.17	*y/D*=1	0.17*D*
Second half	*xy*	*z/D*=0.08	*z/D*=0.92	0.08*D*
	yz	*x/D*=0.17	*x/D*=1	0.17*D*
	zx	*y/D*=1.2	*y/D*=2.03	0.17*D*

Tab. 2 Investigated planes (static and rotating case).

The light sheet, which is generated by a double cavity Nd-YAG laser, has a pulse duration of 6*ns*, a wave length of 532*nm* and a maximum energy per pulse of about 200*mJ*. Seeding is made up of MF-RhB-Particles, whose diameter ranges from 1 to 20μm, that scatter light at a different wavelength so it has been possible, by using a filter, to drastically reduce the spurious reflections. To display, acquire and record digital images, the following items are used: a video camera Kodak Megaplus model ES 1.0 with a CCD sensor (1008×1018 pixels, 256 grey levels); a PC equipped with an acquisition board; a laser-acquisition system synchronizer. By using a digital pick-up sensor it has been possible to synchronize the rotation of the channel with the PIV system acquisition. Tab. 3 reports, both for the static and the rotating case, the principal experimental parameters used to acquire the PIV images relative to the three groups of planes associated to the three coordinate planes (*xy*, *yz*, *zx*).

***xy*-planes**			
Static Case	**# images**	**Delay time**	**Light sheet thickness**
	1000	2000μs	1mm
Rotating case	**# images**	**Delay time**	**Light sheet thickness**
	1000	350μs	1.5mm
***yz*-planes and *zx*-planes**			
Static Case	**# images**	**Delay time**	**Light sheet thickness**
	1000	700μs	1.5mm
Rotating case	**# images**	**Delay time**	**Light sheet thickness**
	1000	350μs	1.5 mm

Tab. 3 Experimental parameters used to the PIV images acquisitions.

The acquired images are interrogated by a high accuracy PIV iterative algorithm based on image deformation method, the detailed description of the steps of the used PIV algorithm is reported in the work of Astarita and Cardone [19]. It has been verified through a statistical investigation that a sample of 1000 images assures the statistical convergence of the three mean velocity components.

For the rotating case, the distributions of the mean velocity component *w* relative to the *xz*-planes have been obtained adopting the following procedure: for every investigated *xz* and *yz* plane, it has been necessary to acquire, besides the 1000 images at *Re*=20000 and *Ro*=0.3, 100 images with the fluid at rest and with the same angular speed and the same delay time between the laser pulses used to obtain the *Ro* equal to 0.3. Indeed the velocity component *w* distributions, with channel in rotation, have been obtained by following relation:

$$w = w_1 - w_2 \tag{3}$$

where w_1 is the mean flow field deduced by the images acquired at *Re*=20000 and *Ro*=0.3 and w_2 is that evaluated by means the images acquired with the rotating channel and with fluid at rest.

3 3D Reconstruction of the flow and vortical field

In order to perform a tridimensional reconstruction of the flow field in the two halves of the turn region, the three groups of distributions of the mean velocity components associated to the three coordinate planes (*xy*, *yz*, *zx*), previously filtered by means of a Wiener filter, have been interpolated on a common tridimensional grid. In this tridimensional domain the distributions of the three velocity components have been obtained by averaging the velocity components distributions which are in common to two of the planes' groups above cited. Besides it has been possible to evaluate for all the slices parallel to the coordinate planes the vorticity's components Ω_x, Ω_y and Ω_z by using the formulae based on Stokes' theorem:

$$\Omega_l = \lim_{s\to 0} \oint_C \frac{\underline{V}\cdot d\underline{l}}{S} \tag{3}$$

where *C* is the circuit containing the surface *S* that is normal to the *l* axis. The Fig. 2 shows the circuit *C*, formed by 8 points, used to obtain the relations 4, 5 and 6 which allow to calculate the three vorticity's components Ω_x, Ω_y and Ω_z.

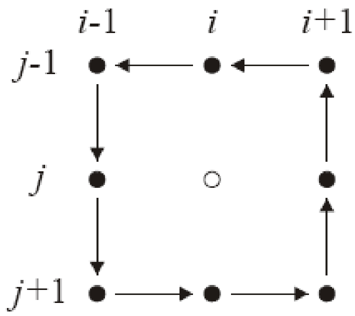

Fig. 2 Circuit used to evaluate Ω_x, Ω_y and Ω_z.

$$\begin{aligned}\Omega_x \approx \frac{1}{4\Delta y\Delta z}\Big[&\Delta z w_{i+1,j} + \frac{1}{2}\Delta z\left(w_{i+1,j-1} + w_{i+1,j+1}\right) - \\ &+\Delta y v_{i,j+1} - \frac{1}{2}\Delta y\left(v_{i-1,j+1} + v_{i+1,j+1}\right) - \\ &+\Delta z w_{i-1,j} - \frac{1}{2}\Delta z\left(w_{i-1,j-1} + w_{i-1,j+1}\right) + \\ &+\Delta y v_{i,j-1} + \frac{1}{2}\Delta y\left(v_{i-1,j-1} + v_{i+1,j-1}\right)\Big]\end{aligned} \tag{4}$$

$$\begin{aligned}\Omega_y \approx \frac{1}{4\Delta z\Delta x}\Big[&\Delta x u_{i+1,j} + \frac{1}{2}\Delta z\left(u_{i+1,j-1} + u_{i+1,j+1}\right) - \\ &+\Delta z w_{i,j+1} - \frac{1}{2}\Delta z\left(w_{i-1,j+1} + w_{i+1,j+1}\right) -\end{aligned}$$

$$
\begin{aligned}
&+\Delta x u_{i-1,j}-\frac{1}{2}\Delta x\left(u_{i-1,j-1}+u_{i-1,j+1}\right)+\\
&\left.+\Delta z w_{i,j-1}+\frac{1}{2}\Delta z\left(w_{i-1,j-1}+w_{i+1,j-1}\right)\right]
\end{aligned}
\tag{5}
$$

$$
\begin{aligned}
\Omega_z \approx \frac{1}{4\Delta x\Delta y}\Bigg[&\Delta y v_{i+1,j}+\frac{1}{2}\Delta y\left(v_{i+1,j-1}+v_{i+1,j+1}\right)-\\
&+\Delta x u_{i,j+1}-\frac{1}{2}\Delta x\left(u_{i-1,j+1}+u_{i+1,j+1}\right)-\\
&+\Delta y v_{i-1,j}-\frac{1}{2}\Delta y\left(v_{i-1,j-1}+v_{i-1,j+1}\right)+\\
&+\Delta x u_{i,j-1}+\frac{1}{2}\Delta x\left(u_{i-1,j-1}+u_{i+1,j-1}\right)\Bigg]
\end{aligned}
\tag{6}
$$

The calculation of Ω_x, Ω_y and Ω_z allowed to plot the volumetric distributions of the adimensional vorticity's module Ω (eq. 7) in the turn region both for the static and the rotating case.

$$
\Omega=\frac{\left(\sqrt{\left(\Omega_x^2+\Omega_y^2+\Omega_z^2\right)}\right)\cdot D}{U_b}
\tag{7}
$$

where D is the hydraulic diameter and U_b is the bulk velocity.

4 Experimental results

In this section the iso-Ω surfaces relative to the second part of the turn region for the static case, and relative both to the first and second part of the turn for the rotating case will be shown. To allow a better description and understanding of these iso-Ω surfaces, some distributions of the mean velocity component w/U_b with the streamlines superimposed relative to the yz and xz planes will be also reported.

4.1 Static case

In Fig. 3 are reported the iso-Ω surfaces relative to Ω=2 (Fig. 3b), Ω=3.5 (Fig. 3c) and Ω=6.5 (Fig. 3d).

Fig. 3b shows two iso-Ω surfaces, with an almost cylindrical shape, which start from the frontal wall and develop along the corners formed by the two side walls and by the external wall; these iso-Ω surfaces, along the flow direction, tend to get together with the two iso-Ω surfaces which face to the two side walls.

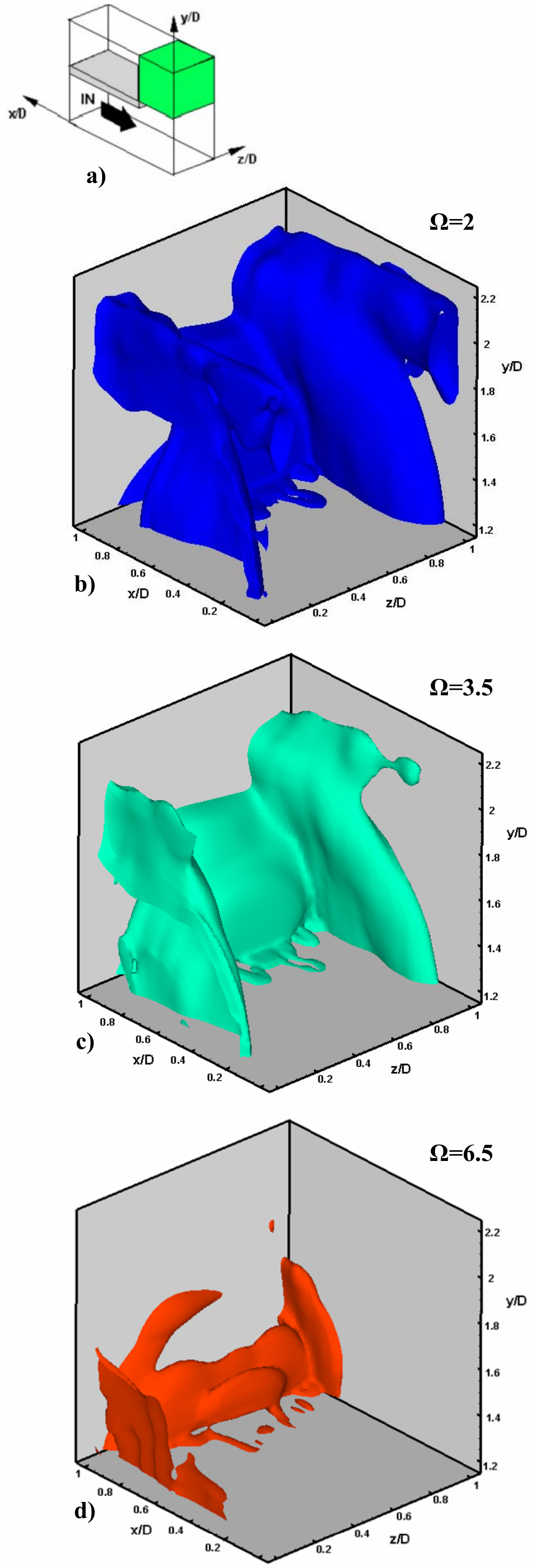

Fig. 3 3D-reconstruction of the vorticity's distribution in the second half of the turn (static case, *Re*=20000): a) sketch of the test region, b) iso-Ω surfaces (Ω=2), c) iso-Ω surfaces (Ω=3.5), d) iso-Ω surfaces (Ω=6.5).

The first two iso-Ω surfaces are associated to the vortices located along the corners formed by the two side walls and by the external wall of the second half of the turn region (Fig. 4). These vortices are a consequence of the impact of the flow, coming from the first part of the turn, on the external wall of the second part of the turn region. Indeed this impact determines in the *yz*-planes a flow bifurcation and consequentially the formation of two counter rotating vortices. The other two iso-Ω surfaces, faced to the two side walls, are due to the Dean vortices which develop owing to the pressure gradient associated to the centrifugal forces present in the turn (Fig. 5). The shape of the two iso-Ω surfaces near the two side walls (Fig. 3c) and the extinction of the Dean vortices near the external wall of the second half of the turn (Fig. 5) let us suppose that these vortices bend and, as observed by Gallo and Astarita [20], persist also in the outlet duct. The Dean vortices are stronger than the ones located along the corners formed by the two side walls and by the external wall of the second half of the turn. Indeed, from Fig. 3c, it is possible to see the extinction of the iso-Ω surfaces in proximity of the frontal wall.

By increasing the vorticity's level (Fig. 3d) it notices that the iso-Ω surfaces tend to collapse on the tip of the partition wall where the shear stresses are strongest.

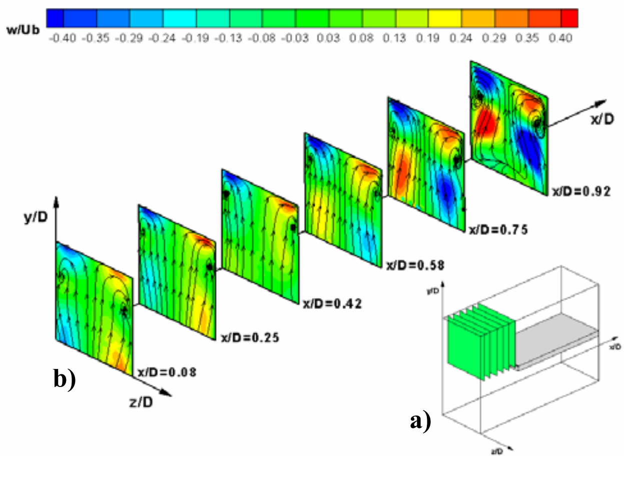

Fig. 4 Secondary flow fields measured in the yz-planes for the static case: a) sketch of the test region with the investigated planes, b) distributions of the mean velocity components w/U_b with the streamlines superimposed.

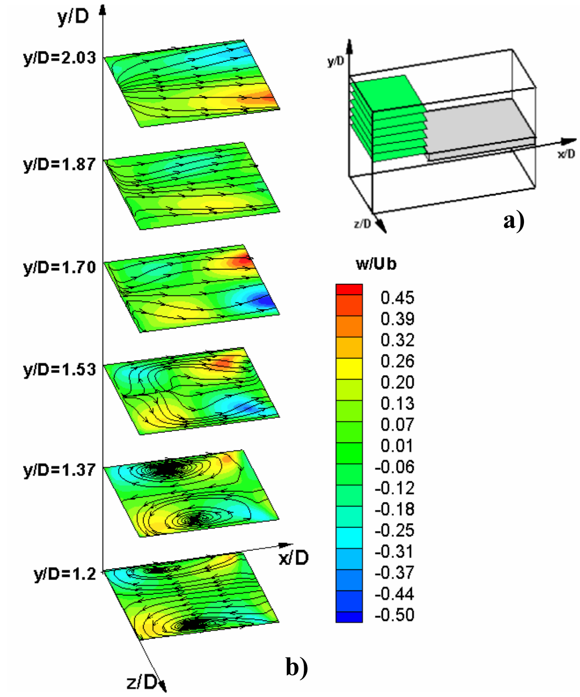

Fig. 5 Secondary flow fields measured in the *zx*-planes for the static case: a) sketch of the test region with the investigated planes, b) distributions of the mean velocity components w/U_b with the streamlines superimposed.

4.2 Rotating case

4.2.1 First half of the turn region

Fig. 6 reports iso-Ω surfaces corresponding to Ω=4.5 and the streamlines relative to the first half of the turn. The more significant aspect that has to be highlighted is the presence of a cylindrical iso-Ω surface which extends near the leading wall (Fig. 6b). As highlighted by the streamlines, this iso-Ω surface is linked to the presence, near the leading wall of the first part of the turn, of a strong vortex. To understand the genesis of this vortex it is necessary to know the behavior of the flow in the inlet duct. In this region the Coriolis' force determines the axial velocity profile asymmetry (Fig 7). Indeed the particles of fluid with higher axial velocity are shifted towards the trailing wall. Therefore the flow from the inlet duct, in the first half of the turn, bumps against the frontal wall near the trailing wall then moves, along the frontal wall, towards the leading wall and finally comes back towards the inlet of the turn (see streamlines, Fig 6b) forming the strong vortex.

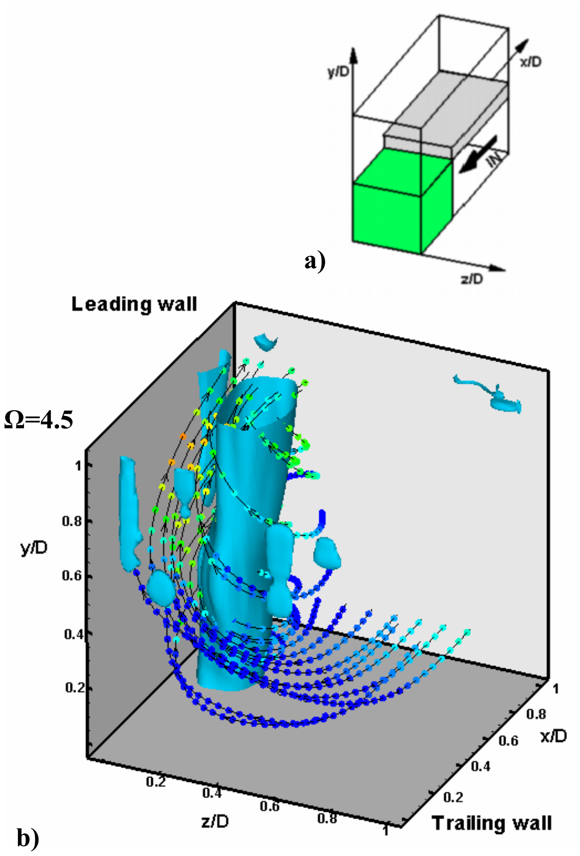

Fig. 6 3D-reconstruction of the vorticity's distribution in the first half of the turn (rotating case, *Re*=20000 and *Ro*=0.3): a) sketch of the test region, b) iso-Ω surfaces (Ω=4.5) and streamlines.

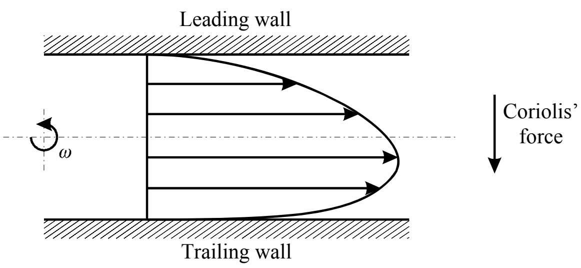

Fig. 7 Axial velocity profile (inlet duct).

4.2.2 Second half of the turn region

Similarly to the static case, the flow coming from the first half of the turn, bumps against the external wall but, in this case, owing to the rotation, the bifurcation's zone is shifted towards the trailing wall and this produce two asymmetric counter rotating vortices positioned in proximity of the angles formed by the external wall and by the leading and trailing wall (Fig. 8). These vortices are identified, in the tridimensional reconstruction of the vorticity's module Ω (Fig. 9b) by the two closed iso-surfaces which start from the frontal wall and extend along the two external corners.

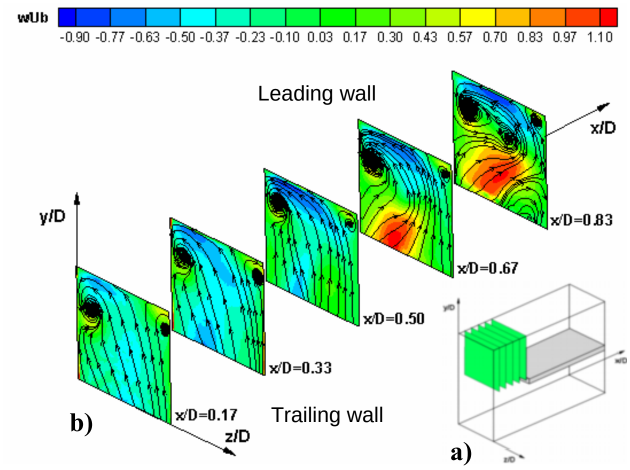

Fig. 8 Secondary flow fields measured in the *yz*-planes for the rotating case (*Re*=20000 and *Ro*=0.3): a) sketch of the test region with the investigated planes, b) distributions of the mean velocity components w/U_b with the streamlines superimposed.

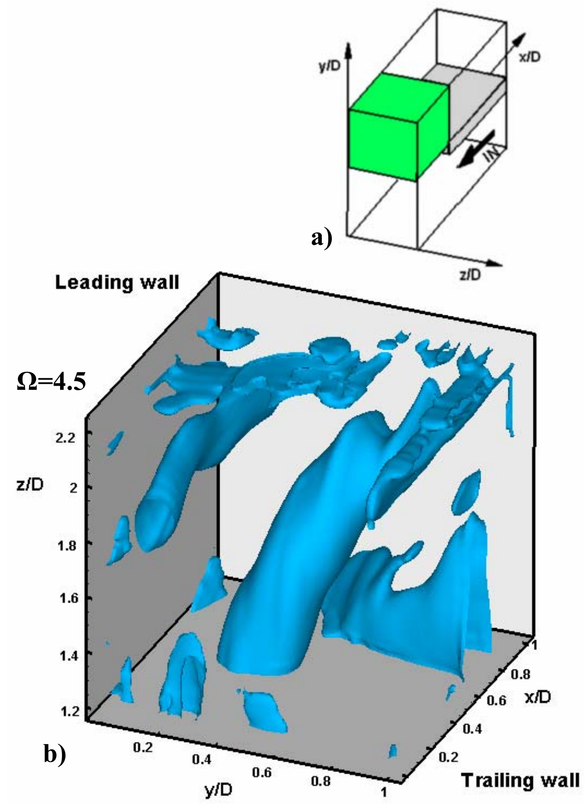

Fig. 9 3D-reconstruction of the vorticity's distribution in the second half of the turn (rotating case, *Re*=20000 and *Ro*=0.3): a) sketch of the test region, b) iso-Ω surfaces (Ω=4.5).

The large vortex positioned, in the first half of the turn near the leading wall, in the second half bends towards the trailing wall. This phenomenon, caused by the zero setting of the Coriolis' force in the turn, determines a strong impinging flow on the trailing wall towards the outlet section of the turn (Fig. 8, x/D=0.83) which causes two vortical structures: the first, formed by two co-rotating vortices, extends along the external wall while the second is located near the lower angle of the trailing wall.

The iso-Ω surface, positioned between the outlet section of the turn and the cylindrical surface which is representative of the large vortex present in the turn region, is associated to the recirculation bubble present immediately after the turn region near the partition wall of the outlet duct. Indeed, in the outlet duct, by moving the xy investigated planes from the leading towards the trailing wall, it has been observed by Gallo et Astarita [20] that the recirculation bubble tend to move upstream entering in the turn region in proximity of the trailing wall.

3 Conclusions

PIV measurements have been performed with the aim both to obtain detailed information about the flow field and to realize a 3D reconstruction of the vortical field in the turn region, with and without rotation.

For the static case, in the second part of the turn region, it has been observed that the flow field is characterized by the presence of two couples of counter rotating vortices. The first couple, located along the corners formed by the two side walls and by the external wall, is generated by the impact of the flow, coming from the first half of the turn, on the external wall of the second half. The second couple, known in literature as Dean vortices, is generated by the pressure gradient associated to the centrifugal forces present in the turn and results to be stronger than the first one.

For the rotating case, in the first half of the turn, it has been observed that the flow field is marked by the presence of a strong vortex which develops along the leading wall. In the second half of the turn, this vortex undergoes a curvature towards the trailing wall. At last the rotation determines an asymmetry of the couple of the vortices which, in the static case, are positioned along the corners formed by the two side walls and by the external wall of the second half of the turn.

References

[1] Kiml R, Mochizuki S and Murata A. Influence of 180 degree sharp turn on the heat transfer and flow behaviour in a smooth square channel cross sectional serpentine channel. *Proc of the 8th International Symposium of Flow Visualization*, 1998.

[2] Liou T-M, Tzeng Y-Y, Chen C-C. Fluid flow in a 180 deg sharp turning duct with different divider thicknesses. *Journal of Turbomachinery*, Vol. 121, pp 569-576, 1999.

[3] Son S Y, Kihm H D and Han J-C. PIV flow measurements for heat transfer characterization in two-pass square channels with smooth and 90° ribbed walls. *International Journal of Heat and Mass Transfer*, Vol. 45, pp 4809-4822, 2002.

[4] Schabacker J, Bolcs A and Johnson B V. PIV investigation of the flow characteristics in an internal coolant passage with two ducts connected by a sharp 180° bend. *ASME* Preprint 98-GT-544, Stockholm, Sweden, 1998.

[5] Cheah S C, Iacovides H, Jackson D C, Ji H and Launder B E. LDA investigation of the flow development through rotating U-ducts. *Journal of Turbomachinery*, Vol. 118, pp 590-596, 1996.

[6] Iacovides H, Jackson D C, Kelemenis G, Launder B E and Yuan Y M. Experiments on local heat transfer in a rotating square-ended U-bend. . *International Journal of Heat and Fluid Flow*, Vol. 20, pp 302-310, 1999.

[7] Liou T-M and Chen C-C. Heat transfer in a rotating two-pass smooth passage with 180° rectangular turn. *International Journal of Heat and Mass Transfer*, Vol. 42, pp 231-247, 1999.

[8] Brossard C, Servouze Y, Gicquel P and Barrier R. Characterization of the flow field inside a rotating, rib-roughened, U-shaped channel using particle image velocimetry. *In Proceedings of 21st International Congress Instrumentation in Aerospace Simulation Facilities*, 2005.

[9] Al-Qahtani M, Jang Y-J, Chen H-C and Han J-C. Flow and heat transfer in rotating two-pass rectangular channels (AR=2) by Reynolds stress turbulence model. *International Journal of Heat and Mass Transfer*, Vol. 45, pp 1823-1838, 2002.

[10] Su G, Chen H-C, Han J-C and Heidmann J D. Computation of flow and heat transfer in rotating two-pass rectangular channels (AR=1:1, 1:2 and 1:4) with smooth walls by a Reynolds stress turbulence

model. *International Journal of Heat and Mass Transfer*, Vol. 47, pp 5665-5683, 2004.

[11] Murata A and Mochizuki S. Large eddy simulation of turbulent heat transfer in a rotating two-pass smooth square channel with sharp 180° turns. *International Journal of Heat and Mass Transfer*, Vol. 47, pp 683-698, 2004.

[12] Iacovides H, Launder B E and Li H-Y. The computation of the flow development through stationary and rotating U-ducts of strong curvature. *International Journal of Heat and Fluid Flow*, Vol. 17, pp 22-33, 1996.

[13] Iacovides H and Raisee M. Recent progress in the computation of flow and heat transfer in internal cooling passages of turbine blades. *International Journal of Heat and Fluid Flow*, Vol. 20, pp 320-328, 1999.

[14] Johnston J P, Hallen R M and Lezius D K. Effects of spanwise rotation on the structure of two–dimensional fully developed turbulent channel flow. *Journal of Fluid Mechanics*, Vol. 56/3, pp 533-557, 1972.

[15] Lezius D K and Johnston J P. Roll–cell instabilities in rotating laminar and turbulent channel flows. *Journal of Fluid Mechanics*, Vol. 77/1, pp 153-175, 1976.

[16] Qin Z and Pletcher R H. Large eddy simulation of turbulent heat transfer in a rotating square duct. *International Journal of Heat and Fluid Flow*, Vol. 27, pp 371-390, 2006.

[17] Gallo M, Astarita T and Carlomagno G M. Heat transfer measurements in a rotating two-pass square channel. *Quantitative InfraRed Thermography Journal*, Vol. 4, No. 1, pp 41-62, 2007.

[18] Kline S C and McClintok F A. Describing uncertainties in single-sample experiment. *Mech Eng*, Vol.75, pp 3-8, 1953.

[19] Astarita T and Cardone G. Analysis of interpolation schemes for image deformation methods in PIV. *Experiments in Fluids*, Vol. 38, pp 233-243, 2005.

[20] Gallo M and Astarita T. PIV measurements in a rotating channel. *In Proceedings of the 7th International Symposium of Particle Image Velocimetry*, Rome, 2007.

Copyright Statement